INTERNATIONAL JOURNAL FOR NUMERICAL METHODS IN FLUIDS, VOL. 14, 403–421 (1992)

COMPUTATION OF WAVES GENERATED BY SUBMARINE LANDSLIDES

M. VERRIERE

Laboratoire de Détection et de Géophysique CEA, BP 12, F-91680 Bruyères-le-Châtel, France

AND

M. LENOIR

Groupe Hydrodynamique Navale CNRS–Paris VI, ENSTA Centre de l'Yvette, Chemin de la Hunière,
F-91120 Palaiseau, France

SUMMARY

Waves generated by submarine landslides are treated as three-dimensional flows of a perfect incompressible fluid. For the solution of the Cauchy–Poisson problem a time-discretization is applied which leads at each time step to a non-homogeneous free surface condition; the solution is then divided into two parts. The first part, subject to the true free surface condition, is computed in a simplified domain with constant depth. The second part involves a homogeneous free surface condition, a corrected bottom condition and the true bathymetry. In the case of constant depth, unconditional stability of the time discretization is derived. In the case of variable depth, mass and energy conservation is derived. Numerical results are presented. Comparison is made with other methods for the generation of axisymmetric waves. The transient propagation along a rectilinear coast is studied, including a comparison between two different bathymetries; trapping of energy is observed.

KEY WORDS Linearized surface waves Three-dimensional Fast Fourier transform Green function Finite element Rectilinear coast

1. INTRODUCTION

Submarine landslides involving large volumes of unstable sediments and rocks can produce water waves of considerable height which propagate over great distances. For instance, at Nice (France) in 1979 a subsidence of nearly 10^7 m^3 of alluvion occurred at the Var river mouth. The resulting wave amplitude was still 3 m when recorded at a distance of 9 km from the perturbation area. A frequent phenomenon is the trapping of energy around an island or along a coast. In such a case an accurate description of the bathymetry and source with respect to space and time is necessary during the initial wave formation as well as during the subsequent propagation. In the present paper three-dimensional linear models are considered within the framework of potential theory and unsteady free surface fluid flows. First our numerical technique is detailed, whose aim is to avoid using the unstationary Green function[1,2] by introducing a time discretization. Then results are presented; comparisons are made with industrial codes in axisymmetric cases, and propagation along a coast is studied for two different shapes of the bathymetry.

0271–2091/92/040403–19$09.50

Received December 1990
Revised April 1991

2. NUMERICAL METHOD

2.1. The linear model

Let (x, y, z, t) denote Cartesian co-ordinates and time with the z-axis pointing in the opposite direction from the gravitational force. The irrotational flow of a perfect and incompressible fluid with an isobaric free surface is considered around an island. The fluid motion being due to some movement of the bathymetry, both the amplitude and slope of the resulting surface waves are assumed to be small, so that infinitesimal wave theory applies. All material displacements being neglected to first order, only submarine ground velocities are transmitted to the water for propagation. The linearized fluid domain consists of the complementary of a three-dimensional bounded set standing for the island in a region limited by two horizontal planes, D being the distance between the planes (Figure 1).

Let us recall the classical dimensionless equations of infinitesimal wave theory,[3]

$$\nabla^2\varphi=0 \quad \text{in } \Omega, \tag{1}$$

$$\partial_n\varphi=\gamma \quad \text{on } \Gamma, \tag{2}$$

$$\partial_z\varphi=0 \quad \text{on } \Gamma_{-1}, \tag{3}$$

$$\partial_{tt}\varphi+\partial_z\varphi=0 \quad \text{on } \Gamma_0, \tag{4}$$

with the following notation (Figure 2):

φ	velocity potential
γ	source term
Ω	fluid domain
Γ	variable depth boundary
Γ_{-1}	constant depth boundary
Γ_0	linearized free surface.

The initial conditions are given by

$$\varphi=0 \quad \text{on } \Gamma_0, \tag{5}$$

$$\partial_t\varphi=0 \quad \text{on } \Gamma_0. \tag{6}$$

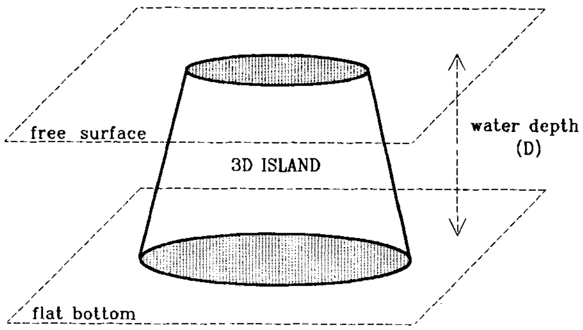

Figure 1. Fluid domain around a three-dimensional island with constant water depth beyond some distance

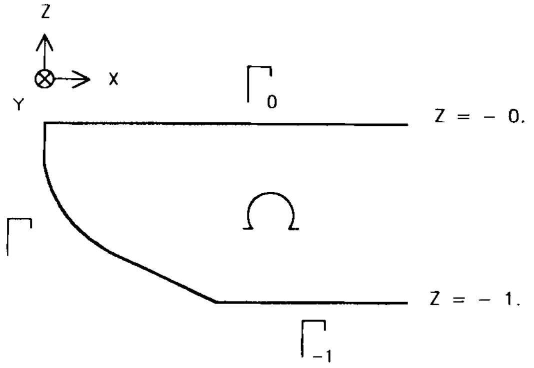

Figure 2. Notation for the dimensionless linearized problem in real geometry

The free surface elevation η is obtained *a posteriori* by means of the relation

$$\eta = -\partial_t \varphi \quad \text{on } \Gamma_0. \tag{7}$$

The length scale is D and the speed scale is $(gD)^{1/2}$, g being the acceleration due to gravity.

Let us point out that equation (2) stands for the source phenomenon, which is taken into account by enforcing the normal velocity component of Γ. Actually the support of γ may be restricted to a subset of Γ.

2.2. *Time discretization*

Let Δt be some constant positive time step. For every integer p, $\varphi^p(x, y, z)$ denotes the approximation of $\varphi(x, y, z, p\Delta t)$ which arises from the solution of the following sequence of problems:

$$\nabla^2 \varphi^p = 0 \quad \text{in } \Omega, \tag{8}$$

$$\partial_n \varphi^p = \gamma(p\Delta t) \quad \text{on } \Gamma, \tag{9}$$

$$\partial_z \varphi^p = 0 \quad \text{on } \Gamma_{-1}, \tag{10}$$

$$\Delta t^{-2}(\varphi^p - 2\varphi^{p-1} + \varphi^{p-2}) + \partial_z[\tau\varphi^p + (1-2\tau)\varphi^{p-1} + \tau\varphi^{p-2}] = 0 \quad \text{on } \Gamma_0. \tag{11}$$

Equation (11) is nothing but a classical centred scheme.[4]

Now the intermediate function

$$\chi^p = \tau\varphi^p + (1-2\tau)\varphi^{p-1} + \tau\varphi^{p-2} \tag{12}$$

fulfils the conditions

$$\nabla^2 \chi^p = 0 \quad \text{in } \Omega, \tag{13}$$

$$\partial_n \chi^p = \gamma^p \quad \text{on } \Gamma, \tag{14}$$

$$\partial_z \chi^p = 0 \quad \text{on } \Gamma_{-1}, \tag{15}$$

$$\partial_z \chi^p + \mu\chi^p = \mu\varphi^{p-1} \quad \text{on } \Gamma_0, \tag{16}$$

with

$$\gamma^p = \tau\gamma(p\Delta t) + (1-2\tau)\gamma[(p-1)\Delta t] + \tau\gamma[(p-2)\Delta t] \quad \text{on } \Gamma, \tag{17}$$

$$\mu = \tau^{-1}\Delta t^{-2}. \tag{18}$$

The initial conditions are

$$\varphi^{-1} = 0 \quad \text{on } \Gamma_0, \tag{19}$$

$$\varphi^0 = 0 \quad \text{on } \Gamma_0. \tag{20}$$

We are then concerned with the numerical calculation of χ^p at each time step. Two different right-hand sides can be found in the χ^p-problem. The first (γ^p) is the source refreshing which is localized on the bounded set Γ, while the second (φ^{p-1}) stands for the wave propagation and tends to spread over the unbounded set Γ_0 as time passes. At each time step the work is divided into two parts, each devoted to one of these two right-hand sides.

One must notice that avoiding the introduction of χ^p would have led to a more complicated expression of the right-hand side in (16), including vertical derivatives of φ^{p-1} and φ^{p-2}.

2.3. *Propagation step*

Throughout the present subsection we leave out the real geometry to consider the whole domain between the two horizontal planes of respective altitudes minus one and zero. This domain ($|\Omega|$) is called the extended fluid domain, while the two planes ($|\Gamma_{-1}|$ and $|\Gamma_0|$) are called the extended constant depth boundary and the extended linearized free surface respectively (Figure 3). Let us now introduce the new function ψ^p which satisfies the following conditions:

$$\nabla^2\psi^p = 0 \qquad \text{in } |\Omega|, \tag{21}$$

$$\partial_z\psi^p = 0 \qquad \text{on } |\Gamma_{-1}|, \tag{22}$$

$$\partial_z\psi^p + \mu\psi^p = \mu\phi^{p-1} \qquad \text{on } |\Gamma_0|, \tag{23}$$

with ϕ^{p-1} being any regular extension of φ^{p-1} from Γ_0 to $|\Gamma_0|$.

The exact solution of the ψ^p-problem is carried out by Fourier transformation with respect to x and y. For any suitable function $f(x, y)$ its transform is denoted $\mathrm{F}f$; one recalls

$$\mathrm{F}f(\xi,\theta) = \int_{-\infty}^{\infty}\int_{-\infty}^{\infty} \mathrm{e}^{-2i\pi(x\xi+y\theta)} f(x,y)\,\mathrm{d}x\,\mathrm{d}y, \tag{24}$$

$$f(x,y) = \int_{-\infty}^{\infty}\int_{-\infty}^{\infty} \mathrm{e}^{2i\pi(x\xi+y\theta)} \mathrm{F}f(\xi,\theta)\,\mathrm{d}\xi\,\mathrm{d}\theta. \tag{25}$$

Assuming integrals (24) and (25) make sense for ϕ^{p-1}, ψ^p and its derivatives, we have

$$\mathrm{F}\psi^p(\xi,\theta,z) = \mathrm{F}\phi^{p-1}(\xi,\theta)\cosh\rho(z+1)/(\rho\sinh\rho + \mu\cosh\rho). \tag{26}$$

with

$$\rho = 2\pi(\xi^2+\theta^2)^{1/2}. \tag{27}$$

Now ψ^p and its derivatives are obtained by means of the inverse Fourier transform.

Two sets of regularly distributed grid nodes are involved in the numerical computations (Figure 4). The first (S) represents the (x, y)-plane and the second (FS) represents the (ξ, θ)-plane.

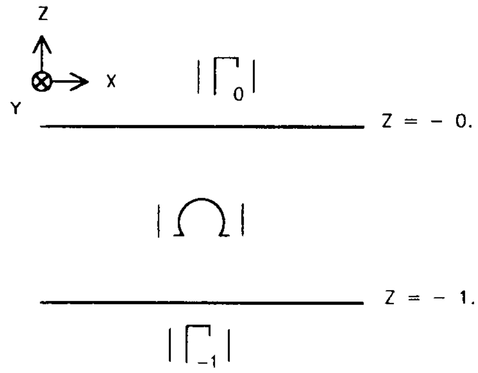

Figure 3. Notation for the propagation step problem in extended geometry; the island is not taken into account

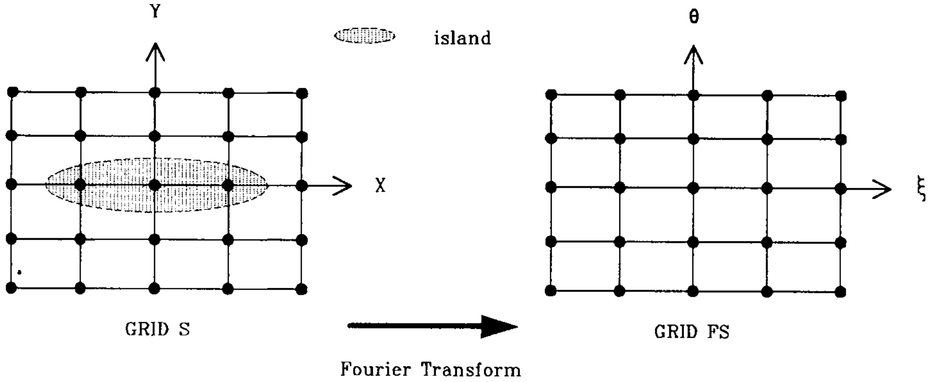

Figure 4. Propagation step grids; extension process information is split into its Fourier components

As soon as an approximation of ϕ^{p-1} (x, y) is known at each point of S, we successively calculate approximate values of

1. (1) $F\phi^{p-1}(\xi, \theta)$ on FS by a direct fast Fourier transform (FFT) algorithm
2. (2) $F\psi^p(\xi, \theta, 0)$ on FS by (26)
3. (3) $\psi^p(x, y, 0)$ on S by an inverse FFT
4. (4) ψ^p and its derivatives at any point (see Section 2.4.3) by evaluating
    - (a) the Fourier transforms of $\psi^p, \partial_x\psi^p, \partial_y\psi^p$ and $\partial_z\psi^p(x, y, z)$ on FS by (26)
    - (b) $\psi^p, \partial_x\psi^p, \partial_y\psi^p$ and $\partial_z\psi^p(x, y, z)$ by (25) and a trapezoidal rule integration on FS.

Let us pay attention to the three following remarks. First, all functions of (x, y) or (ξ, θ) are considered negligible outside the region delimited by S or FS respectively. Secondly, using an FFT is not appropriate in the case (4b), since the results are to be provided for given points which are irregularly distributed, especially on Γ. Thirdly, it can be seen that the propagation step is finally reduced to a two-dimensional problem.

2.4. Generation step

In the present subsection the real geometry is taken into consideration as well as the source characteristics.

2.4.1. Homogeneous free surface condition. Let us now introduce the new function ζ^p such that

$$\chi^p = \psi^p + \zeta^p. \tag{28}$$

From (13)–(16), (21)–(23) and (28), ζ^p is found to fulfil the following system:

$$\nabla^2 \zeta^p = 0 \quad \text{in } \Omega, \tag{29}$$

$$\partial_n \zeta^p = \gamma^p - \partial_n \psi^p \quad \text{on } \Gamma, \tag{30}$$

$$\partial_z \zeta^p = 0 \quad \text{on } \Gamma_{-1}, \tag{31}$$

$$\partial_z \zeta^p + \mu \zeta^p = 0 \quad \text{on } \Gamma_0. \tag{32}$$

It is to be noticed that χ^p does not depend on the way φ^{p-1} is extended from Γ_0 to $|\Gamma_0|$ (see Section 2.3), as opposed to ψ^p and ζ^p which are without physical meaning.

Now one must solve a three-dimensional problem set in an unbounded domain where non-homogeneous conditions are restricted to bounded boundaries. It is thus possible to reduce the computation domain to a bounded one by means of an integral equation or a transparent boundary condition.

To achieve this aim, several methods can be applied, e.g.

(1) the classical boundary element method
(2) the localized finite element method[5-8]
(3) the coupling between finite elements and integral representation.[9,10]

Here the last one is retained, whose qualities are good convergence properties and great flexibility with regard to the choice of a suitable mesh.

2.4.2. The coupling between finite elements and integral representation. Let us recall the main lines of this method. The Green function must first be introduced which satisfies

$$\nabla^2 G_M = \delta_M \quad \text{in } |\Omega|, \tag{33}$$

$$\partial_z G_M = 0 \quad \text{on } |\Gamma_{-1}|, \tag{34}$$

$$\partial_z G_M + \mu G_M = 0 \quad \text{on } |\Gamma_0|, \tag{35}$$

with

$$\delta_M(x, y, z) = \delta(x - x_M) \otimes \delta(y - y_M) \otimes \delta(z - z_M), \tag{36}$$

δ denoting the Dirac measure and M being a point of co-ordinates (x_M, y_M, z_M) such that $-1 < z_M < 0$. The numerical calculation of G_M has been carried out by Cuer:[11]

$$G_M(x, y, z) = -(4\pi)^{-1}\{[r^2 + (z - z_M)^2]^{-1/2} + [r^2 + (z + z_M + 2)^2]^{-1/2}\}$$
$$-(2\pi)^{-1}\int_0^{\infty} [J_0(\rho r)\cosh\rho(z+1)\cosh\rho(z_M+1)\mathrm{e}^{-\rho}(\rho-\mu)/(\rho\sinh\rho+\mu\cosh\rho)]\,\mathrm{d}\rho, \tag{37}$$

with

$$r = [(x - x_M)^2 + (y - y_M)^2]^{1/2}. \tag{38}$$

From Green's formula

$$\int_{\Omega} [(\nabla^2 G_M)\zeta^p - G_M(\nabla^2 \zeta^p)]\,\mathrm{d}v = \int_{\partial\Omega} [(\partial_n G_M)\zeta^p - G_M(\partial_n \zeta^p)]\,\mathrm{d}s, \tag{39}$$

(29) and (31)–(35) the following integral representation is derived:

$$\zeta^p(M) = \int_{\Gamma} [(\partial_n G_M)\zeta^p - G_M(\partial_n \zeta^p)]\,\mathrm{d}s, \tag{40}$$

which is valid for any point M in the interior of Ω.

We now introduce a fictitious boundary Σ surrounding Γ (Figure 5). All unbounded sets Ω, Γ_{-1} and Γ_0 are then divided into two subsets:

1. a bounded one lying between Γ and Σ ($\langle\Omega\rangle$, $\langle\Gamma_{-1}\rangle$ and $\langle\Gamma_0\rangle$ respectively)
2. an unbounded one lying outside Σ ($\rangle\Omega\langle$, $\rangle\Gamma_{-1}\langle$ and $\rangle\Gamma_0\langle$ respectively).

Now the restriction of ζ^p to $\langle\Omega\rangle$ is the solution of a well-posed problem set in a bounded domain and resulting from

1. restricting (29), (31) and (32) to $\langle\Omega\rangle$, $\langle\Gamma_{-1}\rangle$ and $\langle\Gamma_0\rangle$ respectively
2. including (30)
3. writing (40) for each point M on Σ.

To compute the solution of this last problem, a finite element discretization is used. Since a non-local transparent boundary condition couples the two surfaces Γ and Σ, several specific terms are to be added to the classical finite element formulation. Provided that $\Gamma \cap \Sigma$ is empty, the location of Σ is arbitrary, so that the mesh is reduced to a layer of elements around Γ (Figure 6).

Item (3) is a Dirichlet coupling;[2] a Neumann coupling is obtained by applying the operator ∂_n to both sides of (40). In the case of a Dirichlet coupling the degrees of freedom located on Σ are eliminated from the linear system, whose matrix is partly full and asymmetric instead of being sparse and symmetric as in the usual methods. This drawback cannot be avoided as long as the total absorption of numerical reflections on boundaries is required.

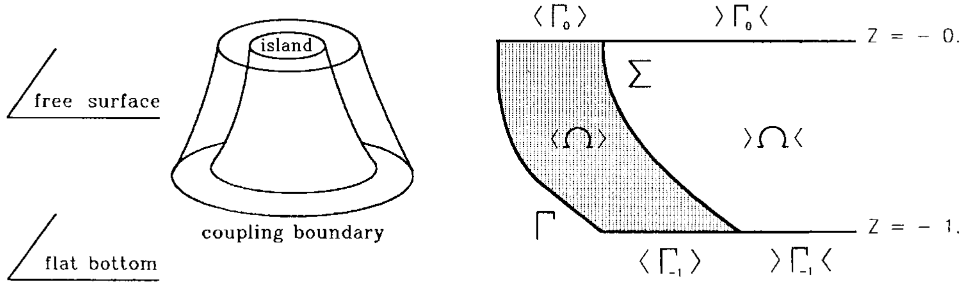

(a) (b)

Figure 5. (a) Arbitrary coupling boundary and (b) corresponding notation

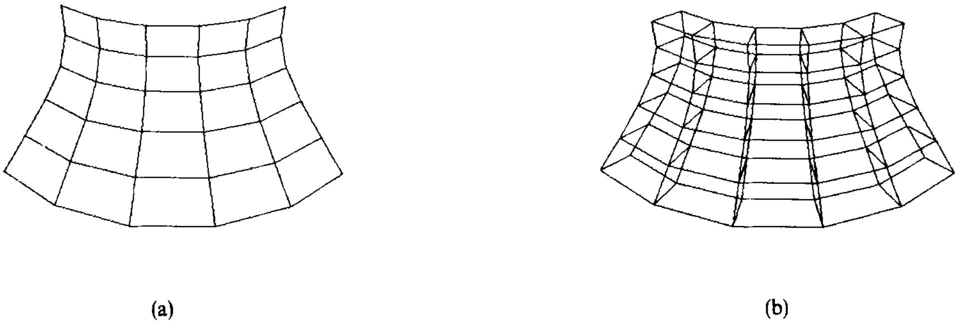
(a)

(b)

Figure 6. (a) Surface gridding of real bathymetry. (b) One-layer finite element mesh for the generation step problem, built from (a)

2.4.3. Plan of computation. Assuming a mesh has been chosen, the computation includes the following three stages:

(1) assembling the right-hand side of the finite element linear system
(2) solving this linear system
(3) restoring the solution on the whole free-surface.

In step (1) approximate values of $\partial_n \psi^p$ are calculated at each mesh point located on Γ (see item (4a) and (4b) of Section 2.3), while exact values of γ^p are calculated at the same points with a given analytical function. All these values are then multiplied by the sum of a $\Gamma \times \Gamma$ mass matrix of classical type and a $\Gamma \times \Sigma$ single-layer matrix of coupling type so as to form the right-hand side of the linear system.

The matrix of the linear system consists of the sum of a $\Omega \times \Omega$ stiffness matrix of classical type and a $\Gamma \times \Sigma$ double-layer matrix of coupling type. Its inverse is calculated once and for all before starting the time loop.

In step (3) an extension Z^p of ζ^p is calculated at each point of S (see Section 2.3) by interpolating two sets of approximate values of ζ^p. The first set, resulting directly from step (2), consists of the approximate values of ζ^p at each mesh point located on $\langle \Gamma_0 \rangle$. The second set consists of the approximate values of ζ^p at points located on $\rangle \Gamma_0 \langle$ and representative of the exterior free surface. These values are obtained by means of the integral representation (40), which involves two terms. For the first term, approximate values of $\partial_n \psi^p$ and exact values of γ^p at each mesh point located on Γ are multiplied by a $\Gamma \times \rangle \Gamma_0 \langle$ single-layer matrix of coupling type. For the second term, approximate values of ζ^p, obtained in step (2), at each mesh point located on Γ are multiplied by a $\Gamma \times \rangle \Gamma_0 \langle$ double-layer matrix of coupling type.

The extension Z^p provides data in the empty area $|\Gamma_0| \setminus \Gamma_0$, then is applied on S:

$$\phi^p = [\psi^p + Z^p - (1-2\tau)\phi^{p-1} - \tau\phi^{p-2}]/\tau, \tag{41}$$

so that the next propagation step is ready to be executed.

Finally, it can be seen that the generation step is reduced to a nearly two-dimensional problem.

2.5. Properties of the numerical scheme

The convergence of the whole method cannot be immediately derived from general results,[12, 13] since both the Fourier analysis and variational approach are combined. However, the following considerations can provide some insight.

2.5.1. Unconditional stability in the case of constant depth. Let us introduce the following initial boundary value problem, which represents transient wave propagation over a flat bottom:

$$\nabla^2\varphi=0 \quad \text{in } |\Omega|, \tag{42}$$

$$\partial_z\varphi=0 \quad \text{on } |\Gamma_{-1}|, \tag{43}$$

$$\partial_{tt}\varphi+\partial_z\varphi=0 \quad \text{on } |\Gamma_0|, \tag{44}$$

$$\varphi=\varphi_0 \quad \text{on } |\Gamma_0| \quad \text{at } t=0, \tag{45}$$

$$\partial_t\varphi=\varphi_1 \quad \text{on } |\Gamma_0| \quad \text{at } t=0, \tag{46}$$

where $\varphi=\varphi(x,y,z,t)$, $\varphi_0=\varphi_0(x,y)$ and $\varphi_1=\varphi_1(x,y)$.

(*a*) *Exact solution.* Recalling the notation of Section 2.3, we have

$$\mathrm{F}\varphi(\xi,\theta,0,t)=\mathrm{F}\varphi_0(\xi,\theta)\cos[\omega(\rho)t]+\mathrm{F}\varphi_1(\xi,\theta)\sin[\omega(\rho)t]/\omega(\rho), \tag{47}$$

with

$$\omega(\rho)=(\rho\tanh\rho)^{1/2}, \tag{48}$$

and in particular

$$\mathrm{F}\varphi(0,0,0,t)=\mathrm{F}\varphi_0(0,0)+\mathrm{F}\varphi_1(0,0)t. \tag{49}$$

Then, with

$$A_-(\xi,\theta)=\tfrac{1}{2}(\mathrm{F}\varphi_0-\mathrm{i}\mathrm{F}\varphi_1/\omega)(\xi,\theta), \tag{50}$$

$$A_+(\xi,\theta)=\tfrac{1}{2}(\mathrm{F}\varphi_0+\mathrm{i}\mathrm{F}\varphi_1/\omega)(\xi,\theta), \tag{51}$$

one obtains

$$\mathrm{F}\varphi(\xi,\theta,0,t)=A_-(\xi,\theta)\mathrm{e}^{\mathrm{i}\omega(\rho)t}+A_+(\xi,\theta)\mathrm{e}^{-\mathrm{i}\omega(\rho)t}. \tag{52}$$

(*b*) *Time-discretized solution.* In the case of constant depth the developments of Section 2.4 are useless. It is easy to see that the method described in Sections 2.2–2.4 is then reduced to the following scheme:

$$\tau\mathrm{F}\varphi^p+[\omega^2/(\omega^2+\mu)-2\tau]\mathrm{F}\varphi^{p-1}+\tau\mathrm{F}\varphi^{p-2}=0 \quad \text{on } |\Gamma_0|. \tag{53}$$

When $\rho=0$, we have

$$\mathrm{F}\varphi^p(0,0,0)=\mathrm{F}\varphi^0(0,0)+p[\mathrm{F}\varphi^1(0,0)-\mathrm{F}\varphi^0(0,0)], \tag{54}$$

which fits (49) well.

When $\rho\neq 0$, it is convenient to denote by x_1 and x_2 the roots of the polynomial

$$\Pi(x)=\tau x^2+[\omega^2/(\omega^2+\mu)-2\tau]x+\tau. \tag{55}$$

For $x_1x_2=1$ the classical stability criterion is fulfilled if and only if x_1 and x_2 have the following form:

$$x_1=\mathrm{e}^{\mathrm{i}\lambda(\rho)}, \qquad x_2=\mathrm{e}^{-\mathrm{i}\lambda(\rho)}, \tag{56}$$

which is true as soon as

$$(\tfrac{1}{4}-\tau)\Delta t^2\omega^2<1. \tag{57}$$

In particular, a class of unconditionally stable schemes is obtained with $\tau \geqslant \frac{1}{4}$. From now on, (57) is assumed to be satisfied.

Then, with

$$A^-(\xi, \theta) = \tfrac{1}{2}[F\varphi^0 - i(F\varphi^1/\sin\lambda - F\varphi^0/\tan\lambda)](\xi, \theta, 0), \tag{58}$$

$$A^+(\xi, \theta) = \tfrac{1}{2}[F\varphi^0 + i(F\varphi^1/\sin\lambda - F\varphi^0/\tan\lambda)](\xi, \theta, 0), \tag{59}$$

we obtain

$$F\varphi^p(\xi, \theta, 0) = A^-(\xi, \theta)e^{ip\lambda(\rho)} + A^+(\xi, \theta)e^{-ip\lambda(\rho)}. \tag{60}$$

(*c*) *Minimization of error.* Now, taking (52) and (60) into consideration, with $t = p\Delta t$, it is clear that $\Delta t\omega$ and λ must be as close as possible in order to minimize numerical dispersion. This can be measured by means of the following two series:

$$2\tau(1-\cos\lambda) = \tau\Delta t^2\omega^2/(\tau\Delta t^2\omega^2+1) = \sum_{n=1}^{\infty}(-1)^{n+1}\tau^n(\Delta t\omega)^{2n}, \tag{61}$$

$$2\tau[1-\cos(\Delta t\omega)] = 2\tau\sum_{n=1}^{\infty}(-1)^{n+1}(\Delta t\omega)^{2n}/(2n)!; \tag{62}$$

(61) follows from (18), (55) and (56), while (62) is derived from the usual cosine series. The two first terms in (61) and (62) are always equal, while the absolute value of the difference between the two second terms is equal to $|\tau(\tau - \frac{1}{12})|(\Delta t\omega)^4$.

This leads to the following two conclusions for the case of constant depth: one obtains

(1) the best precision with $\tau = \frac{1}{12}$
(2) the most accuracy between the unconditionally stable schemes with $\tau = \frac{1}{4}$.

2.5.2. Mass and energy conservation. Let us now go back to the case of variable depth, for which a variational formulation can be derived from (8)–(11). When $\gamma = 0$, for any suitable test function $f(x, y, z)$ we have

$$\int_\Omega \nabla[\tau\varphi^p + (1-2\tau)\varphi^{p-1} + \tau\varphi^{p-2}]\cdot\nabla f\,dv + \int_{\Gamma_0}\Delta t^{-2}(\varphi^p - 2\varphi^{p-1} + \varphi^{p-2})f\,ds = 0. \tag{63}$$

First, choosing $f = \Delta t$, we have $M^p = M^1$ for every integer p, with

$$M^p = \int_{\Gamma_0}\Delta t^{-1}(\varphi^p - \varphi^{p-1})\,ds. \tag{64}$$

Secondly, choosing $f = \varphi^p - \varphi^{p-2}$, we have $E^p = E^1$ for every integer p, with

$$E^p = \int_\Omega \nabla\varphi^p\cdot\nabla\varphi^{p-1}\,dv + \int_\Omega \tau|\nabla(\varphi^p - \varphi^{p-1})|^2\,dv + \int_{\Gamma_0}\Delta t^{-2}(\varphi^p - \varphi^{p-1})^2\,ds. \tag{65}$$

In particular, when $\tau = \frac{1}{4}$, we have

$$E^p = \int_\Omega \tfrac{1}{4}|\nabla(\varphi^p + \varphi^{p-1})|^2\,dv + \int_{\Gamma_0}\Delta t^{-2}(\varphi^p - \varphi^{p-1})^2\,ds. \tag{66}$$

The conservation of mass is expressed by (64), while (65) and (66) are the equivalent for energy.

3. NUMERICAL RESULTS

Let us present some numerical results. First a simple application with constant depth is presented which partly validates the numerical method. Then propagation along a rectilinear coast due to an inshore localized source is considered.

3.1. Free surface displacements above a moving bottom

To test the capacity of our programme to simulate the formation of water waves generated by a motion of the bottom, a comparison was established between three different programmes:

1. PISCES—a two-dimensional finite differences code including non-linear compressible equations in a vertical plane with axisymmetry[14, 15]
2. SOLA-VOF—a two-dimensional finite differences code including free surface Navier–Stokes equations in a vertical plane with axisymmetry[16]
3. MELINA—a three-dimensional finite element and integral representation code with special routines including the features of Section 2.

For PISCES and SOLA-VOF the model is a cylindrical box full of water with a small empty cylinder beneath its bottom (Figure 7). The initial water depth, height and radius of the cylinder are denoted D, H and R respectively. At time $t=0$ water from the box is allowed to fill the cylinder. During the calculation the normal flux through the bottom of the box into the cylinder is recorded. Taking averages in both time and space over that boundary, an equivalent fluid velocity V is found. This velocity is then used as a boundary condition for MELINA (Figure 8), with such a duration T that the total mass flux corresponds to the volume of the cylinder, i.e. $VT=H$. Tests were run with $D=100$, 300 and 500 m, while in all cases H = 100 m and $R=150$ m. For MELINA, D has the same definition as in Section 2.1.

Each of Figures 9–12 gives a comparison between the results of PISCES, SOLA-VOF and MELINA. Figures 9 and 10 show for $D=100$ and 300 m respectively the comparative variations of the trough at the epicentre with respect to time. Figures 11 and 12 show for $D=100$ and 300 m respectively the comparative free surface profiles with respect to the radial distance from the

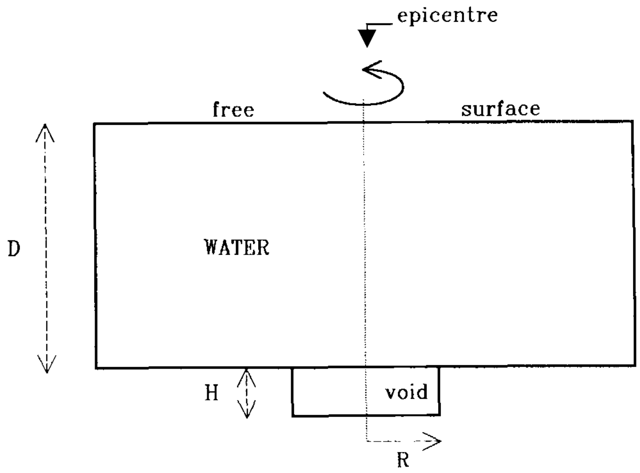

Figure 7. Axisymmetric wave formation model for PISCES and SOLA-VOF

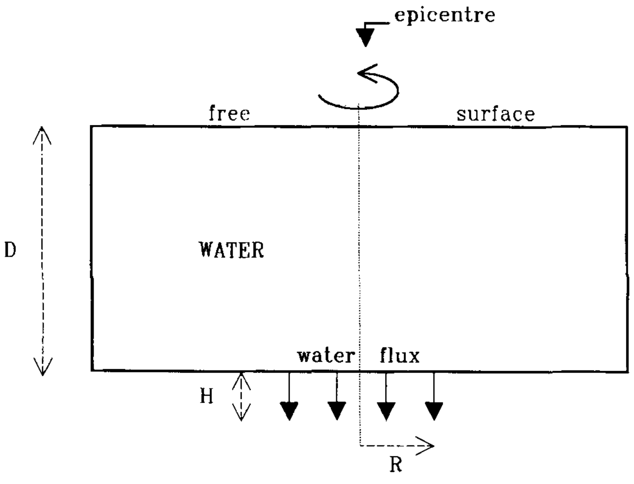

Figure 8. Axisymmetric wave formation model for MELINA

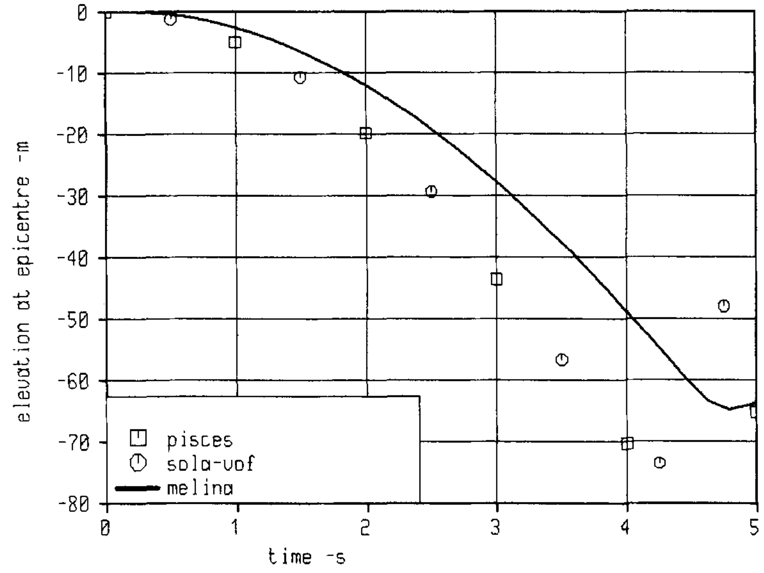

Figure 9. Evolution of trough at epicentre for $D=100$ m

epicentre. All free surface profiles are plotted when the trough is a maximum, which always occurs at the epicentre but not at exactly the same time, depending on each code. All maximum troughs are given in Table I; if α is the ratio of the maximum trough over D, then $\alpha \geqslant 0{\cdot}5$ in the case $D=100$ m, while $\alpha \leqslant 0{\cdot}1$ in the cases $D=300$ and 500 m, where the comparison between free surface profiles is satisfactory. This is in good agreement with the well-known practical linearity criterion $\alpha \leqslant 0{\cdot}1$. The roughness of the source model applied in MELINA does not appear to be very penalizing, since the created waves are not very sensitive to source details.

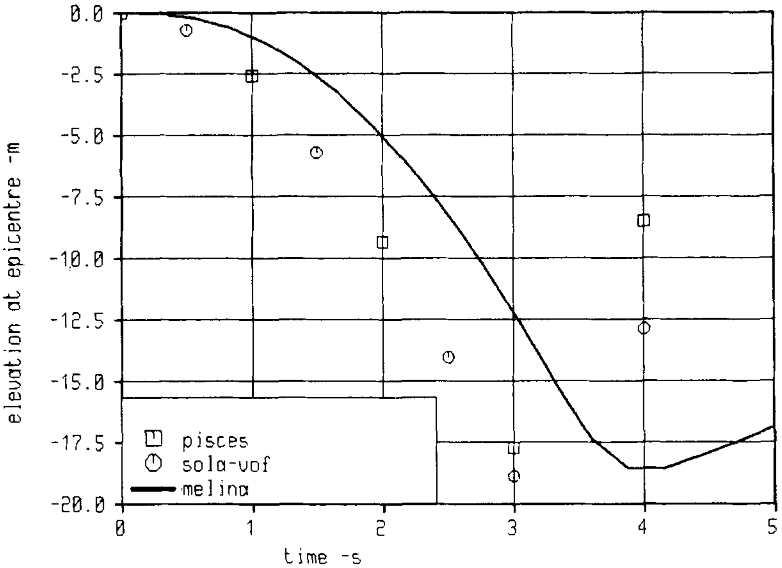

Figure 10. Evolution of trough at epicentre for $D = 300$ m

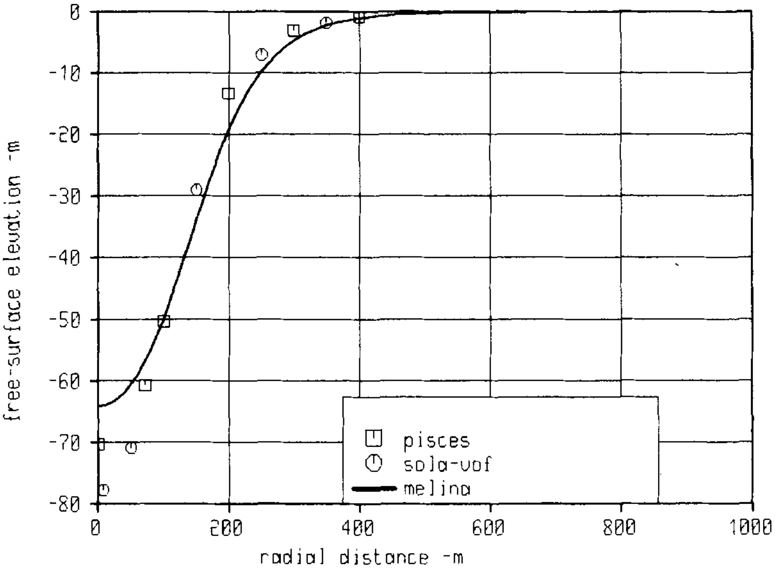

Figure 11. Free surface profile of maximum amplitude for $D = 100$ m

Table I

Code Case	PISCES	SOLA-VOF	MELINA
$D = 100$ m	71 m	78 m	64 m
$D = 300$ m	19 m	19 m	18 m
$D = 500$ m	8 m	8 m	8 m

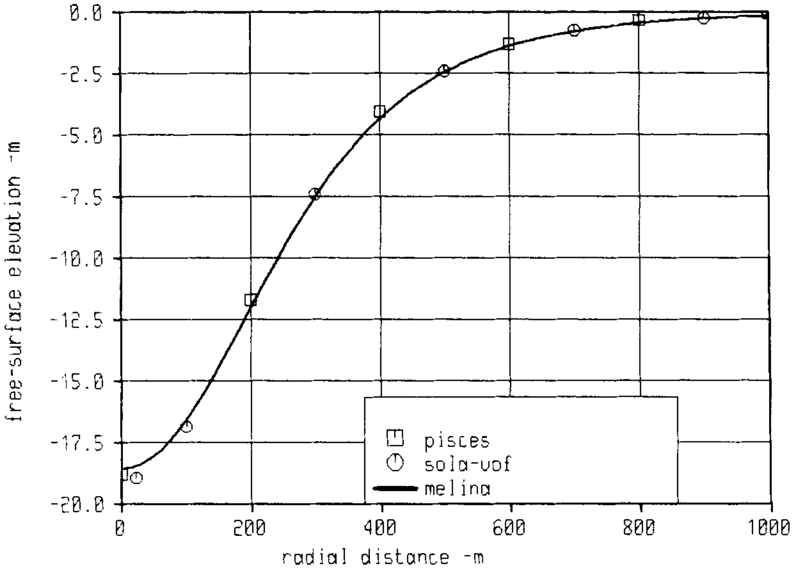

Figure 12. Free surface profile of maximum amplitude for $D = 300$ m

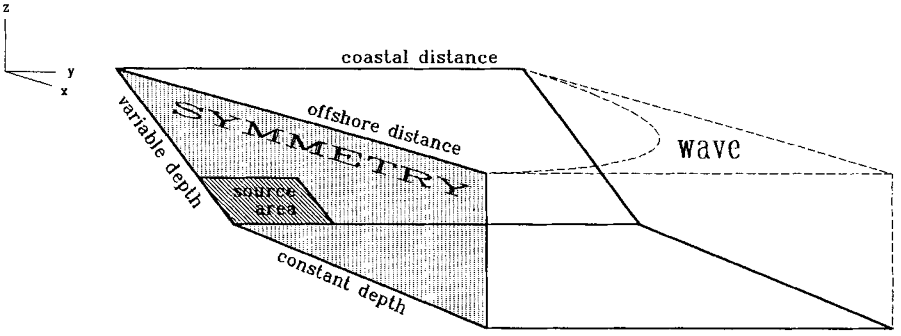

Figure 13. Three-dimensional propagation model along a rectilinear coast

The results of MELINA seem to be validated as long as the linearity hypothesis is justified. However, that validation remains only partial since it is done with a constant depth geometry. In fact, only elements of Section 2.3 have been tested here.

3.2. Propagation along a rectilinear coast

The interest is now focused on more realistic simulations of waves generated by submarine landslides.

3.2.1. The simulations. Throughout the present subsection, $D = 1000$ m (see Section 2.1), so that x, y and z are expressed in kilometres. Invariance of the bathymetry is assumed for any

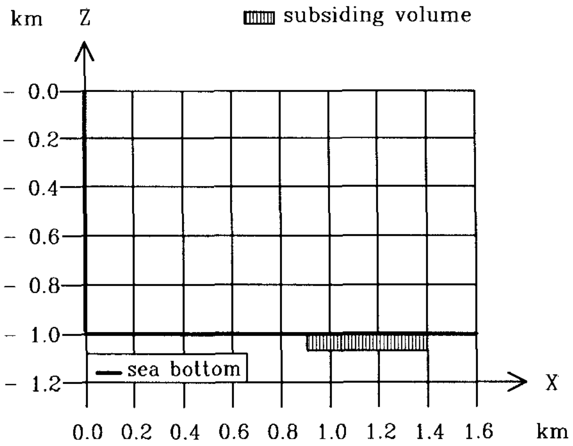

Figure 14. Vertical shape bathymetry

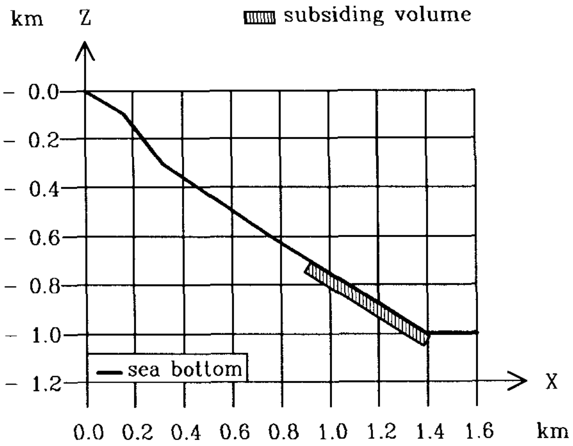

Figure 15. Inclined shape bathymetry

translation parallel to the y-axis, as well as wave symmetry with respect to y. This model can be handled by MELINA if a sufficiently long island is considered.

To show the free surface elevation η, the following notation is used (Figure 13):

$x \geqslant 0$: offshore distance,
$y \geqslant 0$: coastal distance,
η for $x \geqslant 0$ and $y = 0$: offshore wave,
η for $x = 0$ and $y \geqslant 0$: coastal wave,
η for $x \geqslant 0$ and $y \geqslant 0$: wave field.

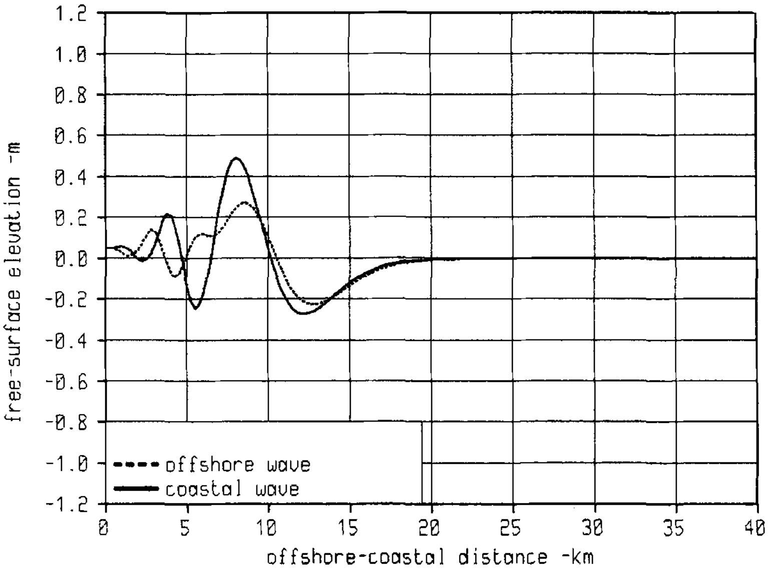

Figure 16. Comparison between offshore wave and coastal wave at 150 s for vertical shape

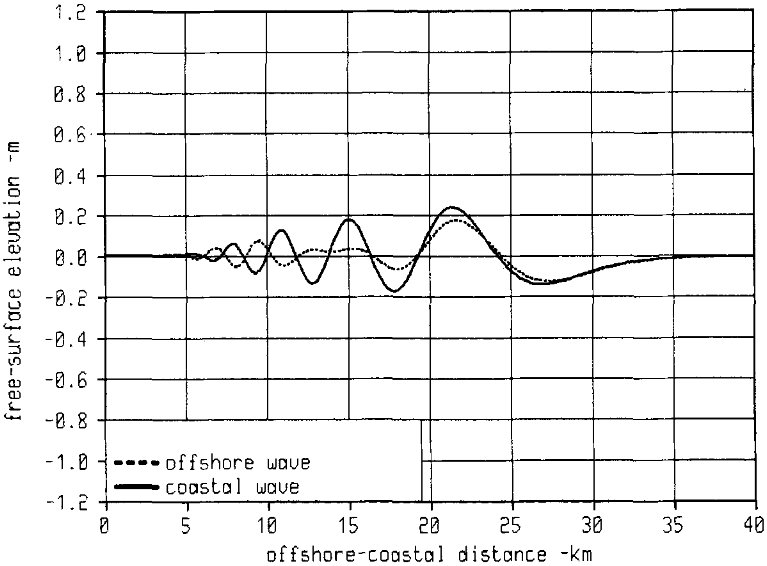

Figure 17. Comparison between offshore wave and coastal wave at 300 s for vertical shape

The bathymetry being defined by its shape in the (x, z)-plane, a comparison was established between a vertical shape and an inclined shape with similar sources (Figures 14 and 15). In both cases the source consists of a subsidence of the sea bottom delimited by $0{\cdot}9 \leqslant x \leqslant 1{\cdot}4$ and $-0{\cdot}3 \leqslant y \leqslant 0{\cdot}3$. The same ground volume of $16{\cdot}2 \times 10^6$ m^3 is assumed to subside within a 30 s

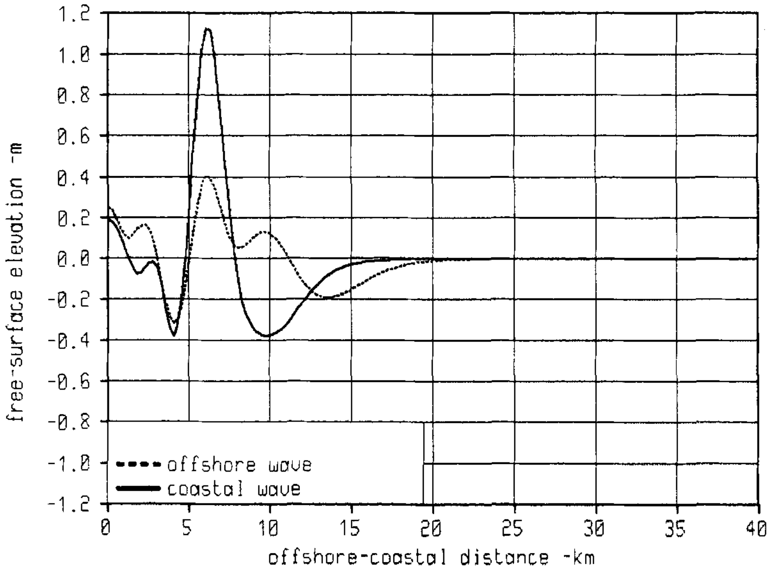

Figure 18. Comparison between offshore wave and coastal wave at 150 s for inclined shape

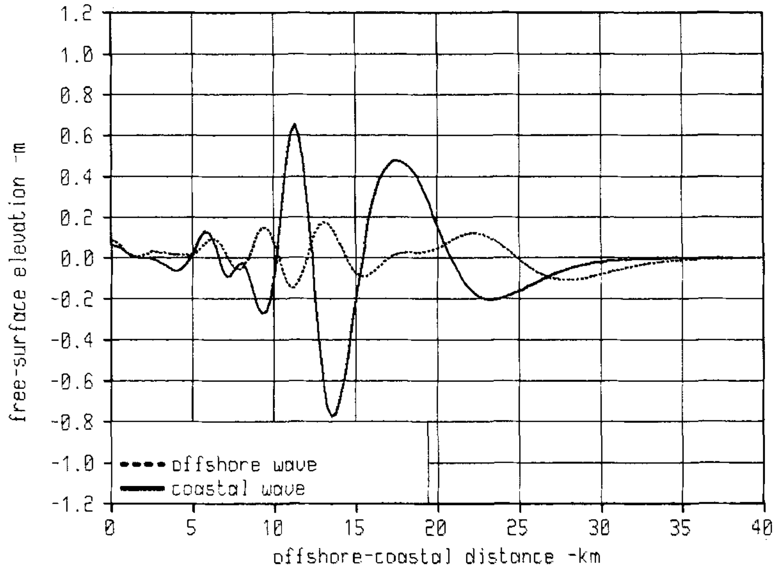

Figure 19. Comparison between offshore wave and coastal wave at 300 s for inclined shape

duration. For the vertical shape a normal velocity of 1·8 m s^{-1} is applied uniformly over a horizontal rectangular bottom area of 500 m by 600 m with 1000 m water depth. For the inclined shape a normal velocity of 1·5 m s^{-1} is applied uniformly over an inclined square bottom area of 600 m by 600 m with water depth between 700 and 1000 m.

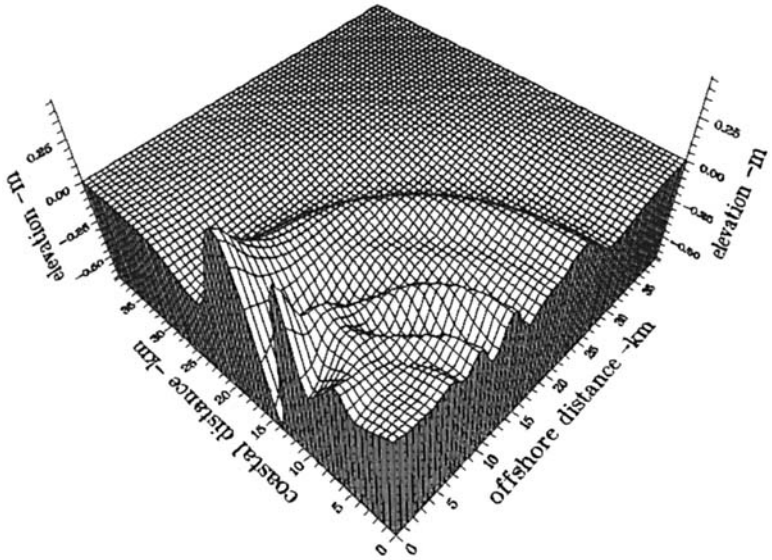

Figure 20. Wave field at 300 s for inclined shape

Figures 16–19 compare offshore and coastal waves after 150 and 300 s of propagation for both shapes. Figure 20 shows a perspective view of the wave field after 300 s of propagation for the inclined shape.

Let β be the ratio of maximum crest to trough in a coastal wave over the same in an offshore wave. For the vertical shape it is found that $\beta = 1{\cdot}6$ at 150 s and $\beta = 1{\cdot}4$ at 300 s; the wave field tends to become spherical. For the inclined shape it is found that $\beta = 2{\cdot}1$ at 150 s and $\beta = 4{\cdot}5$ at 300 s; energy is trapped near the shore.

This phenomenon is classical. In particular, when studying periodic waves with respect to both coastal distance and time, spectral theory shows that many rectilinear coasts are waveguides.[17, 18]

3.2.2. Computational cost. The computational cost was the same for both shapes. The two-dimensional grid used for the propagation step contains 300 × 300 points, no symmmetry being taken into account. The three-dimensional mesh used for the generation step comprises 1000 nodes, all symmetries being taken into account. With such grid and mesh refinements, 3×10^6 words are necessary to entirely run the application in the main memory of a CRAY-XMP computer. The result of Figure 20 is reached after 60 cycles, which took 2 h of CRAY-XMP computation time. These performances can undoubtedly be improved in a large way by FORTRAN optimization.

4. CONCLUSIONS

Within the framework of free surface linear hydrodynamics, a new computation method has been introduced. The discretization technique gives the velocity potential at each point of a wide free surface. This is realized by means of repeated fast Fourier transformation of the two-dimensional wave field, while a fixed three-dimensional free surface piercing object is taken into account by coupling finite elements and integral representation. In this way the convolution term with respect to time is avoided which appears when using methods based on the unstationary Green function. Thus calculations can be done over longer periods.

In the case of a wave generated by an axisymmetric source located on a flat ocean bottom, the results are in good agreement when in the linearity domain with those obtained from the two-dimensional, non-linear, compressible or Navier–Stokes, finite differences codes. Three-dimensional propagation tests show that energy can be trapped along a coast. For a realistic shape of the bathymetry the amplitude of a coastal wave reaches more than four times that of an offshore wave. Therefore a three-dimensional approach is absolutely necessary when dealing with the propagation of water waves in real cases.

A possible application of the technique which has been presented lies in the simulation of tsunami generation from submarine earthquakes. This phenomenon can indeed be considered linear when it occurs at sufficient depth.

REFERENCES

1. A. Jami, 'Etude théorique et numérique de phénomènes transitoires en hydrodynamique navale', *Thèse*, Université Pierre et Marie Curie, Paris, 1981.
2. G. Pot, 'Etude théorique et numérique des mouvements libres de corps flottants et immergés. Extension au cas des grands mouvements de corps immergés', *Thèse*, Ecole Nationale Supérieure de Techniques Avancées, Paris, 1986.
3. J. V. Wehausen and E. V. Laitone, 'Surface waves', in *Encyclopedia of Physics, Vol. 9*, Springer, Berlin, 1960, pp. 446–778.
4. R. Dautray and J. L. Lions, *Analyse Mathèmatique et Calcul Numèrique pour les Sciences et les Techniques, Vol. 3*, Masson, Paris, 1985, pp. 907–931.
5. K. J. Bai and R. Yeung, 'Numerical solution of free-surface flow problems', *Proc. Tenth Symp. on Naval Hydrodynamics*, Cambridge, MA, 1974, pp. 609–647.
6. H. S. Chen and C. C. Mei, 'Oscillations and waves forces in a man-made harbour in the open sea', *Proc. Tenth. Symp. on Naval Hydrodynamics*, Camdridge, MA, 1974, pp. 573–596.
7. K. J. Bai, 'A localized finite element method for steady two-dimensional free-surface flow problems', *Proc. First. Int. Conf. on Numerical Ship Hydrodynamics*, Gaithersburg, MD, 1975, p. 209.
8. M. Lenoir and A. Tounsi, 'The localized finite element method and its application to the two-dimensional sea-keeping problem', *J. Numer. Anal.*, **25**, 729–752 (1988).
9. M. Lenoir and A. Jami, 'A variational formulation for exterior problems in linear hydrodynamics', *Comput. Methods Appl. Mech. Eng.* **16**, 341–359 (1978).
10. M. Lenoir, 'Méthodes de couplage en hydrodynamique navale et application à la résistance de vagues bidimensionnelle', *Thèse*, Université Pierre et Marie Curie, Paris, 1982.
11. M. Cuer, 'Computation of a Green's function for the three-dimensional linearized transient gravity waves problem', *Impact Comput. Sci. Eng.* **1**, 313–325 (1989).
12. P. A. Raviart, 'Multisteps methods and parabolic equations', *France–Japan Seminar on Functional and Numerical Analysis*, Kyoto, 1976; H. Fujita, ed., Japan Society for the Promotion of Science, 1978, pp. 429–454.
13. E. Godlewski, and A. Puech-Raoult, 'Equations d'évolution linéaires due second ordre et méthodes multipas', *RAIRO, Anal. Numér.*, **13**, 329–353 (1979).
14. M. Wilkins, 'Calculation of elastic–plastic flow', *Lawerence Livermore Laboratory Report UCRL-7322, Rev. 1*, 1969.
15. B. Van Leer, 'Towards the ultimate conservative difference scheme. IV. A new approach to numerical convection', *J. Comput. Phys.*, **23**, 276–299 (1977).
16. B. D. Nichols, C. W. Hirt and R. S. Hotchkiss, 'SOLA-VOF: a solution algorithm for transient fluid flow with multiple free boundaries', *Los Alamos Scientific Laboratory Report LA-8355*, 1980.
17. R. M. Garipov, 'Unsteady waves above the submerged ridge', *Dokl. Akad. Nauk, SSSR* **161**, 547–550 (1965) (in Russian).
18. D. V. Evans and T. MacIver, 'Edges waves over a shelf, full linear theory', *J. Fluid Mech.*, **142**, 79–95 (1984).